Fluorescent molecular rotors

From working principles to visualization of mechanical contacts

Suhina, T.

5

Polarity-dependent Excited State Deactivation of DCDHF Molecular Rotors*

Abstract

This chapter builds upon the experiments that we described in Chapter 4. Here we perform additional mechanistic studies on the previously introduced DCDHF-based molecular rotor in order to examine and quantify the influence of solvent polarity on the photophysical behavior of this molecule. In order to systematically examine the influence of solvent polarity on Stokes shifts and fluorescence quantum yields we perform variable-temperature experiments in 2-methyltetrahydrofuran and ethyl acetate, and room temperature experiments in toluene/acetonitrile solvent mixtures. The obtained experimental data clearly point towards the presence of two polarity-responsive excited-state deactivation barriers, in excellent agreement with our previously proposed model and the unusual trends in fluorescence quantum yields reported in Chapter 3 for the same chromophore.[1] We demonstrate that the presence of two excited-state deactivation pathways results in discontinuous dependence of the nonradiative decay rates on polarity at low viscosities. The fluorescence quantum yield is low in non-polar solvents and polar solvents, but reaches a maximum > 0.1 in low-viscosity solvents of moderate polarity. Vis-pump/vis-probe measurements performed in a range of non-polar and polar solvents show excellent agreement with the model that was proposed in Chapter 4, and enable us to capture the transient spectrum of the twisted intermediate.

* T. Suhina, D. Bonn, A. M. Brouwer. Manuscript in preparation.

5.1 Introduction

In the previous chapter we have shown that the fluorescence deactivation pathway of **1** is different in polar and non-polar solvents. Excited-state deactivation proceeds either through twisting of the dicyanomethylene (γ) double bond or through twisting of a formally single (β) bond (Scheme 5.1), where the latter results in formation of the dark twisted intramolecular charge-transfer (TICT) intermediate.[2] In non-polar solvents, excited state deactivation of **1** occurs by twisting of the γ bond. TD-DFT calculations predict that the difference in energy between the ground and excited state of **1** decreases as the γ twist progresses, which ultimately results in surface crossing and ground-state repopulation. As the environment polarity increases, the energy barrier leading towards γ-twisted geometries increases, because the molecular dipole moment of **1** decreases as the γ-twist progresses. The energy barrier towards β-twisted geometries, on the other hand, becomes lower with increasing solvent polarity. This is because β-twist leads to a highly polar twisted intramolecular charge-transfer (TICT) intermediate through which **1** can nonradiatively decay to the ground state. In solvents of medium polarity, the energies of the TICT state and the LE state are comparable, and this results in reversible interconversion between the LE and the TICT states. This leads to delayed fluorescence observed for **1** in medium-polar EtOAc. As the environment polarity increases further, the energy of the TICT state relative to the energy of the LE state is lower and this hinders back-conversion to the fluorescent locally excited state so that it is no longer competitive with the decay to the ground state.[2]

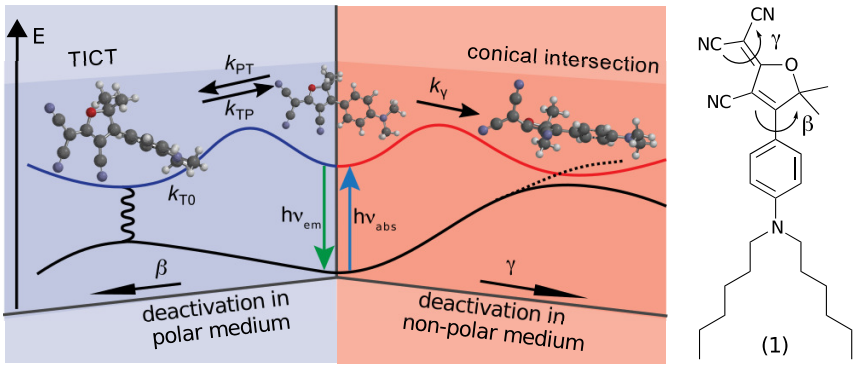

Scheme 5.1: Schematic representation of excited state decay pathways of **1**.

In Chapter 4 (and ref. 2) we demonstrate that solvent polarity greatly influences the excited-state photophysics of **1**. In this chapter we supplement our previous findings, as we attempt to systematically study how fluorescence deactivation of **1** responds towards changes in solvent polarity and provide new evidence for formation of the dark TICT intermediate. In the first part of this Chapter, we use temperature-induced dielectric changes of the surrounding environment (2-

methyltetrahydrofuran, MTHF) to quantify Stokes shifts and fluorescence quantum yields of **1** in a representative medium-polar solvent. Next, we measure fluorescence quantum yields of **1** in EtOAc, and compare these measurements with reaction rates that we reported in Chapter 4. Both experiments are fully consistent with our previously proposed excited-state decay model in solvents of medium polarity, and the latter one demonstrates that excited-state decay occurs exclusively through the β-twisted intermediate in EtOAc. Next, we explore the fluorescence response of **1** over a wider polarity range by measuring fluorescence intensities and fluorescence decays in solvent mixtures as a function of macroscopically observed dielectric properties. Finally, we perform vis-pump/vis-probe measurements in order to reconstruct the species associated spectra of the TICT state and explore fluorescence deactivation of **1** in non-polar, medium-polar, and highly-polar solvents.

5.2 Experimental details

Most of the techniques used here are described in Chapter 2 of this thesis. Experimental details that are specific for this chapter are provided below. All solvents used were of spectroscopic grade and dried over molecular sieves, unless otherwise mentioned. Synthesis of compound **1** is described elsewhere.[3]

5.2.1 Low-temperature experiments

Low-temperature measurements of **1** in MTHF were carried out in a nitrogen-cooled optical cryostat (DN1704, Oxford Instruments) with feedback controller unit (ITC4, Oxford Instruments). An additional thermocouple was placed inside the cuvette containing the sample to ensure that the temperature within the cuvette is fully equilibrated with the temperature in the cryostat. The concentration of the chromophore was adjusted to give an absorbance in 1 cm below ~ 0.1 at the excitation wavelength of 460 nm.

5.3 Results and discussion

5.3.1 Temperature experiments in MTHF

A major fundamental drawback of dielectric continuum-based models lies in their inability to account for specific solute-solvent interactions. This results in a large scatter when Stokes shifts are plotted against the solvent's orientational polarization function, which describes the effect of molecular reorientation in the field of the solute dipole.[4] Throughout this work, we use modified orientational polarization function, $d_c(\epsilon) - d_c(n^2)$, which additionally accounts for solute polarizability (see Chapter 2.1.5 for details).[5,6] In order to minimize influence of specific interactions, the solvent polarity can be regulated by changing the temperature of the system. We chose MTHF for our experiments, as its dielectric properties show a

reasonably large temperature dependence and it forms a clear glass at ~ 137 K.[7,8] The latter allows us to observe the effect of solvent freezing on fluorescence properties of compound **1**. We note that the polarity of MTHF (relative permittivity $\epsilon = 7.0$) is very similar to that of ethyl acetate (relative permittivity $\epsilon = 6.1$),[9] in which reversible interconversion between the fluorescent locally excited (LE) and the dark twisted intramolecular charge-transfer (TICT) state occurs.[2] Dielectric properties of MTHF as a function of temperature are shown in Appendix 5.4.1. Solvatochromic data previously obtained for **1** in pure solvents[2] show excellent agreement with molecular dipole moments obtained from (TD) DFT calculations, and show that the (fluorescent) locally excited state has a pronounced charge-transfer character which leads to larger Stokes shifts with increasing solvent polarity. In MTHF we observe trends that are remarkably different, because Stokes shifts decrease with solvent polarity.

Measured excitation and emission spectra of **1** in MTHF as a function of temperature are shown in Figs. 5.1 a) and b), respectively. The excitation spectra are normalized (Fig. 5.1), and were used to correct for differences in sample absorbances when monitoring fluorescence intensities (see below). The excitation spectra measured below the freezing temperature (T_m) of MTHF become sharper and exhibit a pronounced vibrational structure. We attribute this to reduced inhomogeneous broadening.[4,10,11] Positions of the maxima are shown in Figs. 5.1 c) and d). The emission spectra gradually shift towards lower energies with cooling, up to the point where T_m is reached at which spectra suddenly shift to higher energies. Below T_m, the solvent freeze-out effect is observed, and this imposes a severe limitation on solvent reorientation, which is necessary for a complete excited-state stabilization. This results in the blue shift of the emission peak relative to that in the liquid phase (Fig. 5.1 d)).

Interestingly, excitation energies decrease more steeply than emission energies when cooling the solution of **1** in MTHF. This produces a negative slope when Stokes shifts are plotted against the temperature-regulated solvent polarity function (slope of -2048 ± 729 cm^{-1}, Fig. 5.2). In principle, such an unusual trend could be explained if significant changes in molecular electronic structure would be responsible for lowering $\vec{\mu}_\mathrm{e} - \vec{\mu}_g$ with increasing solvent polarity.[8,10,12] As this is not the case (see Chapter 4[2] and text below) we attribute this to partial relaxation of the solvation shell. Partial relaxation takes place due to solvent reorientation speed decrease with cooling, which leads to incomplete solvation of the excited state at low temperatures.

Both excitation and emission spectra narrow with cooling, but this is more pronounced in case of the emission bands, as shown in Fig. 5.3. Narrowing of both excitation and emission spectra is expected, due to decrease of inhomogeneous broadening at lower temperatures. Below T_m, both excitation and emission spectra narrow more steeply due to severe restrictions in intramolecular and solvent motion imposed by the rigid environment.

Fluorescence intensities exhibit the expected trend throughout the most part of the examined temperature range (Fig. 5.4): as the environment becomes more polar (lower temperatures), fluorescence intensities initially decrease due to in-

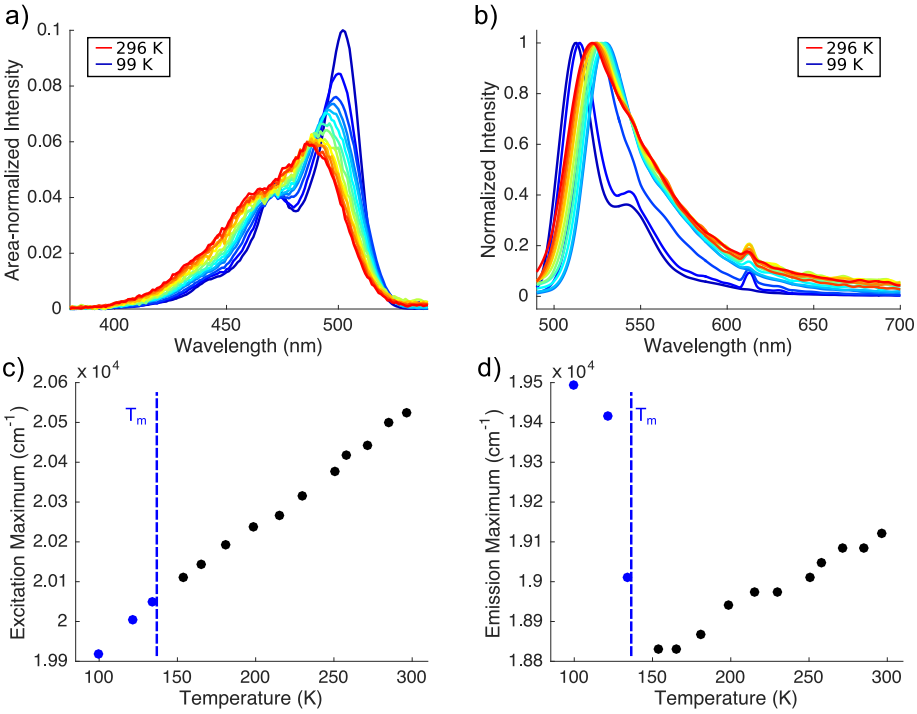

Figure 5.1: a) Area-normalized excitation spectra (λ_{exc} = 460 nm) of **1** in MTHF at different temperatures; b) Normalized emission spectra (λ_{mon} = 560 nm); c) Location of excitation maximum as a function of temperature; d) Location of emission maximum as a function of temperature.

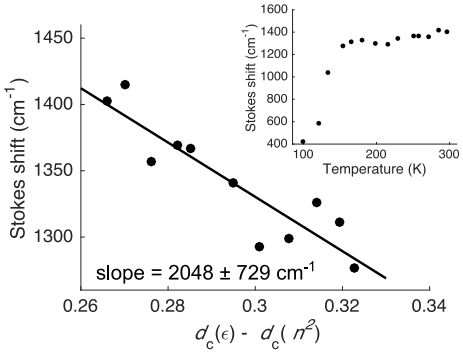

Figure 5.2: Stokes shifts of **1** in MTHF as a function of solvent polarity. Inset shows Stokes shifts as a function of temperature.

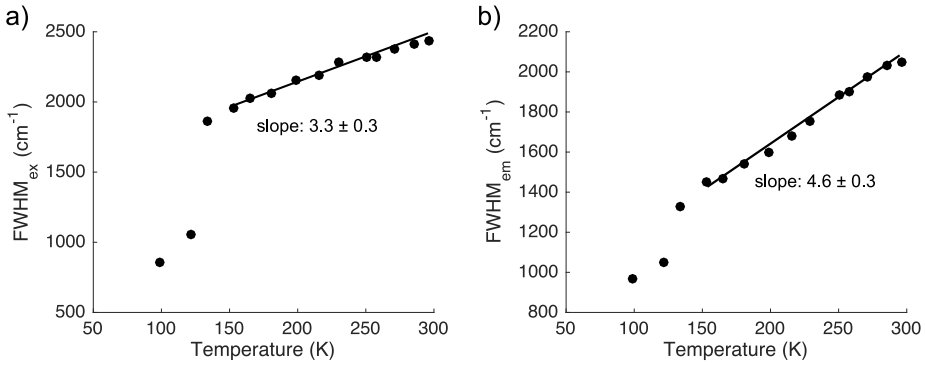

Figure 5.3: Full width at half maximum (FWHM) of **1** as a function of temperature: a) Excitation spectra; b) Emission Spectra.

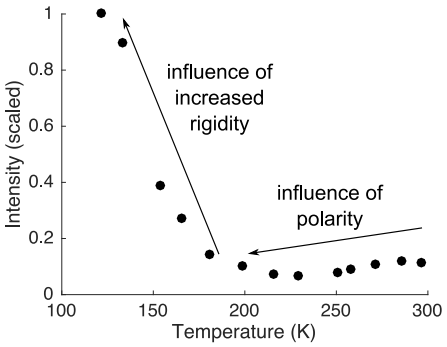

Figure 5.4: Fluorescence intensities ("absorbance" corrected) of **1** in MTHF normalized by the total intensity measured at 99 K as a function of temperature.

creased population of the dark TICT state (Fig. 5.4), in good agreement with our previously proposed model.[2] This occurs in spite of the fact that the viscosity of MTFH increases from 0.46 cP at 298 K to 1.46 cP at 215 K, and demonstrates that solvent polarity has a larger influence on excited-state decay of **1** than viscosity. Upon freezing, the available free volume becomes insufficient to form the dark TICT state efficiently and fluorescence intensities (fluorescence quantum yields, Φ_f) experience a significant enhancement. Interestingly, Φ_f still do not reach unity. Assuming that Φ_f ~2.5 % for **1** in room temperature MTHF ($\Phi_f = 0.025$ in THF, which has a very similar dielectric permitivitty[9]), we estimate the fluorescence quantum yield of **1** to be ~23 % in frozen MTHF matrix. This indicates that formation of the TICT state (or γ-twist), although less efficiently, still occurs.

5.3.2 Variable-temperature experiments in EtOAc

In Chapter 4 we described fluorescence decay measurements of **1** in medium-polar EtOAc at different temperatures, and used a two state model (Scheme 5.1, left) in which the fluorescent LE state reversibly converts into the dark TICT state. We inferred that fluorescence deactivation of **1** in EtOAc takes place exclusively

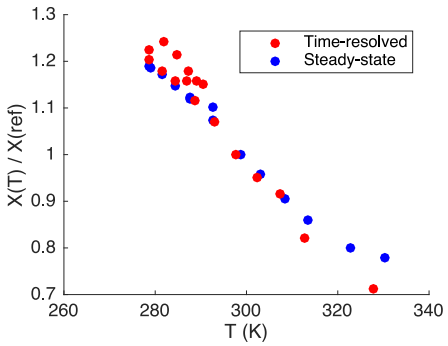

Figure 5.5: Comparison of the results for **1** in EtOAc obtained by steady-state and time-resolved modelling described in Chapter 4.

through formation of the dark TICT state intermediate, in other words, γ twist does not play an important role in the excited state deactivation of **1** in this solvent. We reached this conclusion based on the fact that fluorescence quantum yields show a steady increase with temperature, which is not expected if a competing temperature or a free volume-dependent excited-state deactivation process (such as γ-twist) takes place. Here, we use the same model and express it through equations derived in Chapter 2.1.4 in order to use steady-state fluorescence data to eliminate the possibility of excited state deactivation through the alternative channel (γ twist).

Steady-state data allow us to express the ratio of two derived temperature-dependent quantities ($X(T)/X(T_{\mathrm{ref}})$) as a function of fluorescence quantum yields. Here, $X(T) = [k_{\mathrm{PT}}(T)\ k_{\mathrm{T0}}(T)]/[(k_{\mathrm{TP}}(T) + k_{\mathrm{T0}}(T))]$. The expression we use in our analysis is:

$$\frac{X(T_{\mathrm{x}})}{X(T_{\mathrm{ref}})} = \frac{k_{\mathrm{PT}}(T_{\mathrm{x}})\ k_{\mathrm{T0}}(T_{\mathrm{x}})}{X(T_{\mathrm{ref}})\ (k_{\mathrm{TP}}(T_{\mathrm{x}}) + k_{\mathrm{T0}}(T_{\mathrm{x}}))} = \frac{1 - r(T_{\mathrm{x}})\,\Phi_{\mathrm{f}}(T_{\mathrm{ref}})}{r(T_{\mathrm{x}})\ (1 - \Phi_{\mathrm{f}}(T_{\mathrm{ref}}))},$$

where r represents the ratio of fluorescence quantum yields measured at given and reference temperatures ($r(T_{\mathrm{x}}) = \Phi_{\mathrm{f}}(T_{\mathrm{x}})/\Phi_{\mathrm{f}}(T_{\mathrm{ref}})$). Derivation of this expression is shown in Chapter 2.1.4.[13] . If additional excited state deactivation of **1** would play a significant role, a disagreement between the steady-state and time-resolved derived temperature-dependent quantities $X(T)$ is expected. As shown in Fig. 5.5, excellent agreement between the steady-state and time-resolved measurements makes it safe to conclude that excited state deactivation of **1** in EtOAc proceeds through formation of the dark TICT intermediate, and is not influenced by the deactivation pathway associated with the γ-twisting coordinate.

5.3.3 Titration experiments in solvent mixtures

In order to gain additional understanding of fluorescence deactivation of **1** as a function of environment polarity, we examine the fluorescence response of **1**

in mixtures of polar and non-polar solvents. We chose toluene as non-polar co-solvent, and examined the fluorescence response by titrating toluene solutions of **1** with MeOH, DMSO and MeCN as polar co-solvents. It must be kept in mind that solvent mixtures are rather complex, and the influence of specific interactions/solvation is difficult to asses.[4] Nevertheless, the results presented below show excellent agreement (at least on a semi-quantitative level) with the model shown in Scheme 5.1 and elaborated in Chapter 4.

Because refractive indices (used in quantum yield calculations) and dielectric constants have, to our knowledge, not been reported for mixtures of toluene and MeOH or DMSO, we use the following approximations to estimate these quantities:

$$\epsilon(\text{mixture}) = x\ \epsilon(\text{co-solvent}) + (1-x)\ \epsilon(\text{toluene}), \tag{5.1}$$

$$n(\text{mixture}) = x\ n(\text{co-solvent}) + (1-x)\ n(\text{toluene}), \tag{5.2}$$

where x is the volume fraction of the co-solvent used in a particular experiment. For toluene/MeCN mixtures, we use interpolation based on the experimental data reported in refs. 14 and 15. As mentioned above, the reported bulk-averaged values and our interpolations are mere approximations of dielectric quantities experienced by **1** in solvent mixtures, and do not account for possible specific interactions with the chromophore itself. Fluorescence quantum yields plotted as a function of the full dielectric response of the solvent $d_c(\epsilon)$,[5,6] are shown in Fig. 5.6. Starting from toluene, fluorescence quantum yields show an initial increase with addition of a polar co-solvent. We attribute this rise to the increase of the polarity-sensitive energy barrier that separates the fluorescent LE state from the conical intersection (γ-twist barrier). As the environment polarity increases further, the deactivation pathway through formation of the β-twisted TICT state becomes energetically accessible (once $d_c(\epsilon) \approx 0.36$). This causes fluorescence quantum yields to reach a peak value and decrease further as the TICT deactivation pathway becomes more accessible with further increasing solvent polarity.

In spite of the obtained trends being consistent regarding the $d_c(\epsilon)$ at which Φ_f reach their peak values, the values of Φ_f differ from one system to another. The reason behind this is not clear, but such differences are likely to result from specific interactions that take place between the chromophore and the polar co-solvent. Whatever the underlying cause for such differences may be, the obtained data clearly demonstrate the presence of two different excited-state deactivation barriers that respond differently to changes in solvent polarity. In case of **1** in toluene/DMSO mixtures, the environment viscosity increases ($\eta_{\text{toluene}} = 0.56$ mPa s; $\eta_{\text{DMSO}} = 1.99$ mPa s), in the case of toluene/MeOH ($\eta_{\text{MeOH}} = 0.54$ mPa s) the bulk viscosity remains constant, while in the case of toluene/MeCN ($\eta_{\text{MeCN}} = 0.37$ mPa s) mixtures it decreases with increasing polar solvents fraction.[9] The appearance of plateau in fluorescence quantum yields at $d_c(\epsilon) \approx 0.36$ in case of all the examined solvent mixtures indicates that effects of solvent polarity have a dominant influence on Φ_f of **1** in the low-viscosity regime. Our preliminary results shown in the Appendix to this Chapter (see Chapter 5.4.4) indicate that another widely-used viscosity sensor, 9-(2,2-dicyanovinyl)julolidine (DCVJ), shows trends that are similar to **1** in toluene/DMSO mixtures.

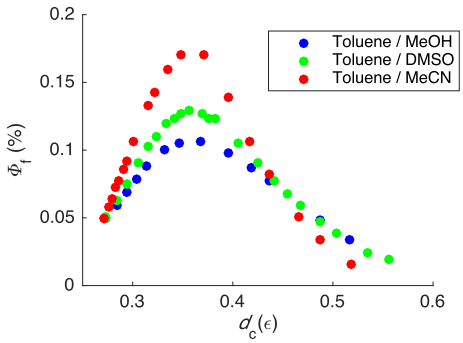

Figure 5.6: Fluorescence quantum yields of **1** *vs* solvent polarity function $d_c(\epsilon)$ obtained in solvent mixtures.

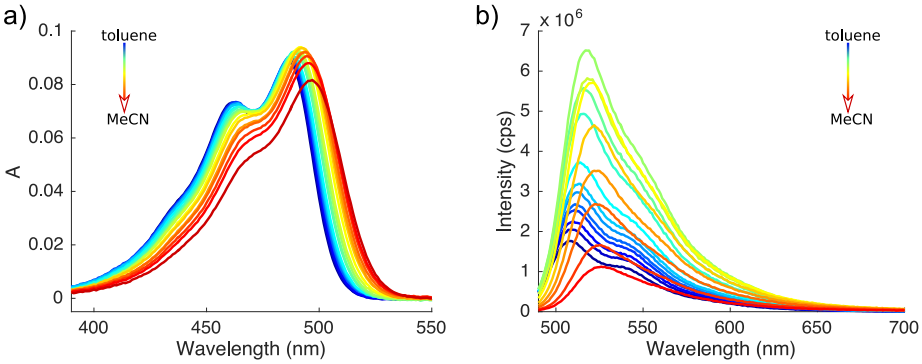

Figure 5.7: a) Absorption spectra of **1** in pure toluene (blue), toluene/MeCN mixtures, and pure MeCN (red); b) Fluorescence emission spectra (absorbance corrected) of **1** in pure toluene (blue), toluene/MeCN mixtures, and pure MeCN (red)

Since the refractive indices and dielectric constants have only been reported for toluene/MeCN mixtures, we focus on steady-state and time-resolved experiments in these mixtures to understand the role of solvent polarity in excited-state deactivation of **1**. With increasing environment polarities, spectral changes characteristic for charge-transfer systems (solvatochromic shifts and disappearance of vibrational structure with increasing solvent polarity)[4] are observed (Fig. 5.7). In toluene/MeCN mixtures, spectral shifts follow the trends obtained in pure solvents. Stokes shifts plotted *vs* solvent's orientational polarization function $d_c(\epsilon) - d_c(n^2)$ are shown in Fig. 5.8. The obtained difference between the excited-state and ground-state dipole moments obtained from a linear fit to the data shown in Fig. 5.8 is $\Delta\mu = 3.8$ D, which is somewhat lower from the values that we have previously obtained for pure solvents ($\Delta\mu = 5.8$ D).

To learn more about the polarity-dependent excited state dynamics of **1** over

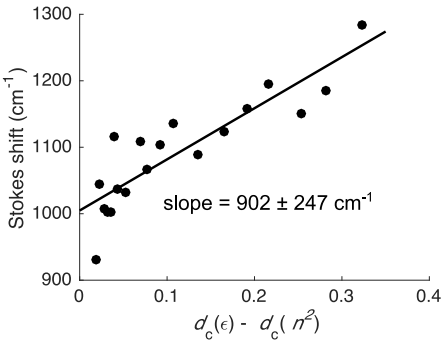

Figure 5.8: Stokes shifts of **1** in toluene/MeCN mixtures *vs* solvent polarity function $d_c(\epsilon) - d_c(n^2)$.

a relatively wide polarity range, we have measured fluorescence decays of **1** in toluene/MeCN mixtures. Representative TCSPC curves are shown in the Appendix, Fig. 5.18. As long as the fluorescence deactivation of **1** proceeds exclusively through the β-twisted intermediate, analytical expressions that are based on a system of partial differential equations that can be written for the respective concentrations of species can be derived and solved for the unknowns. The final expressions that need to be solved are described in the previous chapter and assume the form of the following equations:[16]

$$k_{1/2} = \frac{X + Y \pm (\sqrt{X^2 - 2XY + Y^2 + 4k_{\mathrm{PT}}k_{\mathrm{TP}}})}{2} \tag{5.3}$$

$$A_1 = \frac{X - k_2}{k_1 - k_2}; A_2 = 1 - A_1 \tag{5.4}$$

where A_1, A_2 are the amplitudes associated with fluorescence decay rate constants k_1 $(1/\tau_1)$ and k_2 $(1/\tau_2)$, $X = k_{\mathrm{rad}} + k_{\mathrm{PT}}$, $Y = k_{\mathrm{TP}} + k_{\mathrm{T0}}$ and k_{PT}, k_{TP} and k_{T0} are reaction rates illustrated in Scheme 5.1. When **1** deactivates through both γ and β twist, unique solutions can not be obtained, because the fluorescence decay curves provide only three parameters, while there are four unknowns if $k_\gamma > 0$.

In order to illustrate the influence of competing decay through the γ-twisting channel on reaction rates ($k_{\mathrm{PT}}, k_{\mathrm{TP}}$ and k_{T0}) obtained from the equations above, we will simulate some decays and calculate the respective rates from Eqs. 5.3 and 5.4. This enables us to examine how the γ-twisting deactivation pathway influences the calculated rates when γ twist is not accounted for by our model.

We generate the simulated concentration profiles in the following way. We assign fixed values to the relevant reaction rates: $k_{\mathrm{PT}} = 2.53 \times 10^{10}$, $k_{\mathrm{TP}} = 4.78 \times 10^9$ and $k_{\mathrm{T0}} = 5.83 \times 10^9$ s^{-1}. These values, which were previously obtained from fluorescence decays of **1** in EtOAc at room temperature (293 K), are used here for illustrative purposes. The γ-twisting rates k_γ were fixed to the values

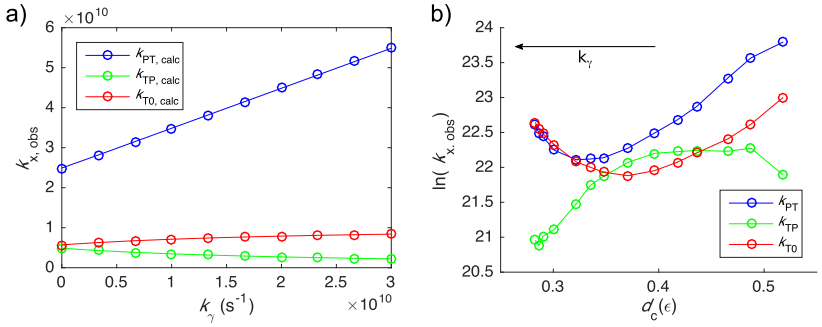

Figure 5.9: a) Calculated rates obtained from Eqs. 5.3 and 5.4 applied to simulated data *vs* γ-twisting rate; b) Calculated rates of **1** obtained from Eqs. 5.3 and 5.4 applied to experimental data measured in toluene/MeCN mixtures *vs* solvent polarity function.

ranged from 0 (as in room temperature EtOAc) and 3×10^{10} s^{-1} (γ-twisting rate becomes similar to β twisting rate). According to the model illustrated in Scheme 5.1, the concentration of the fluorescent species that would be observed in fluorescence decay measurements can be obtained by solving a set of coupled differential equations (the radiative decay rate can be ignored for the sake of simplicity):

$$\frac{\partial[P]}{\partial t} = -k_\gamma[P] - k_{\mathrm{PT}}[P] + k_{\mathrm{TP}}[T], \tag{5.5}$$

$$\frac{\partial[T]}{\partial t} = k_{\mathrm{PT}}[P] - k_{\mathrm{TP}}[T] - k_{\mathrm{T0}}[T], \tag{5.6}$$

Solving these equations for concentration of the planar state (P) allows us to simulate the concentration profile of the planar fluorescent species as a function of time ($P(t)$) with reaction rates defined above. The concentration of this species is directly proportional to fluorescence intensity that we observe in fluorescence decay measurements. By varying k_γ while keeping the other rates constant and subsequently solving for the unknown (calculated, k_{calc}) rate constants by solving Eqs. 5.3 and 5.4, we can see how the apparent rate constants are influenced by changes in k_γ. Results of such simulations are shown in Fig. 5.9 a), in which all the reaction rates (except k_γ) were known and kept constant. The first thing to be noted in Fig. 5.9 a) is that when k_γ is increased the apparent $k_{\mathrm{PT,calc}}$ increases (although k_{PT} in the model was kept constant). This is expected, as the γ twist opens up the additional decay channel for the depopulation of the planar LE state, and this reflects in $k_{\mathrm{PT,calc}}$. The influence on the other calculated rates as the γ-twisting channel opens is less obvious. The simulation shows that increasing k_γ results in slightly decreased $k_{\mathrm{T0,calc}}$ values and a more substantial decrease of $k_{\mathrm{TP,calc}}$.

The results of applying Eqs. 5.3 and 5.4 to experimental fluorescence decay curves of **1** in toluene/MeCN mixtures are shown in Fig. 5.9 b). As the solvent

becomes more polar, the rate contants k_{T0} and k_{PT} are expected to increase, while k_{TP} is expected to decrease with increasing solvent polarity due to stabilization of the highly polar twisted intermediate. For $d_c(\epsilon) > 0.38$ we indeed observe this trend. For lower values of $d_c(\epsilon) < 0.38$ decay through γ-twist is not negligible, and the decay rate constants are overestimated, as expected based on the simulation in Fig. 5.9 a). Because of the small deviation from exponential decay in this regime, the parameters cannot be very accurately derived from the data. The presented data confirm our explanation (Chapter 4) for the unusual trend in fluorescence quantum yields reported in Chapter 3 for identical chromophore.

5.3.4 Vis-pump/vis-probe transient absorption measurements

To obtain further insight into the excited-state deactivation of **1**, we conduct a series of transient absorption measurements of **1** in solvents of low (hexane and toluene), medium (EtOAc) and high polarity (DMSO). In these experiments, we perturb the samples with a pulse of visible light (488 nm), record transient spectra in visible regime at different delays with respect to the pump pulse, and store the gathered spectra in a matrix. Such matrices are then modeled using a compartmental (or target) analysis approach with R package TIMP[17] interfaced through Glotaran[18] and home-built Matlab scripts. Standard errors for estimated rate constants reported here were produced by Glotaran.

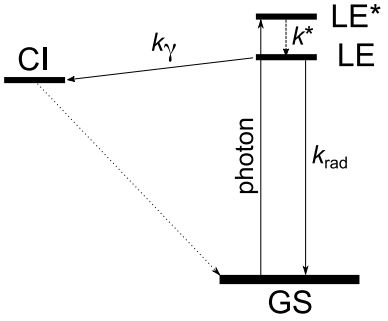

Scheme 5.2: Proposed model for excited-state deactivation of **1** through conical intersection (CI) in non-polar solvents.

Hexane. In transient data obtained for **1** in hexane (Fig. 5.10) we can distinguish three spectral regions: excited-state absorption (ESA), ground-state bleach (GSB) and stimulated emission (SE). A set of transient spectra measured at different probe delays after the pump pulse is shown in Fig. 5.10 a). We attribute the positive transient signal located at higher energies (405-440 nm) to excited-state absorption (ESA). Although excited-state kinetics of **1** in hexane is remarkably fast, the ground-state bleach signal of **1** in hexane located at $\sim 440-500$ nm does not fully recover during the examined time window (3600 ps). This points towards the presence of some dark state (see Fig. 5.10 a) and 5.10 b)). The SE decays

very rapidly, and single-trace fits produce two time constants, which we attribute to vibrational cooling and decay of the locally-excited state.

Global analysis of the whole transient data matrix produces three time constants of $\tau_1 = 0.3$ ps, $\tau_2 = 8.9$ ps and $\tau_3 \sim 8.5$ ns (the longest time constant could not be determined accurately, as the time-traces do not decay to zero in the examined time window). We associate the obtained time constants with the vibrationally hot locally excited (LE*) state, relaxed locally excited (LE) state and a semi-dark state, respectively. The reconstructed decay-associated difference spectra (DADS) obtained by such procedure is shown in Fig. 5.10 c). Stimulated emission and excited-state absorption, although very weak, remain present during long delay times. Amplitudes produced by global fit of the transient data matrix associated with time constants τ_2 and τ_3 in ground-state bleach region indicate that only a small fraction (6-10 %) of the total population forms such a semi-dark state.

At this point, the nature of a long-lived semi-dark state and potential causes for its formation deserve some consideration. The long-lived semi-dark state might be present because of triplet formation, aggregate formation, or photobleaching. The works conducted by Moerner's group demonstrate that single molecules of **1** in rigid polymer matrices (PMMA) do not show pronounced blinking behavior,[19–23] which indicates that triplet formation does not play a significant role in photophysics of **1**. Triplet formation and its decay might, however, take place on time-scales that were not achievable by such experiments. Steady-state data do not show concentration-dependent broadening and spectral shifts in the examined concentration range, which would be expected if aggregate formation would proceed to a significant degree. We do, however, need to keep in mind that formation of both triplets and aggregates is easy to miss if only a small fraction of the total population undergoes such processes (as the experiments suggest for our case). Photobleaching and photoproduct formation present another likely cause for this component. Although we did not observe a significant difference in absorption spectra taken before and after the measurement, the available data does not allow us to eliminate the possibility of sample decomposition or excited state reaction. Earlier in this chapter, we have demonstrated that photophysical behavior of **1** in non-polar toluene significantly changes upon addition of even small amounts of polar solvents. This would suggest that a small amount of impurities might result in fractional population of the TICT state. This, however, can not explain the appearance of the semi-dark state in hexane, as its lifetime is far too long to be associated with the TICT state that we observe in polar solvents and solvent mixtures.

Whatever the underlying reason for this component might be (triplet, aggregates, or some other process), it would need to be accounted for in our model in order to reconstruct the species-associated difference spectra. As the origin of this species is unclear, we limit ourselves to "simple" global analysis which does not assume any specific model. As only a small fraction of total excited-state population forms a semi-dark state, reaction rate constants associated with formation of such state must be slow compared to the ones defined by the sequential

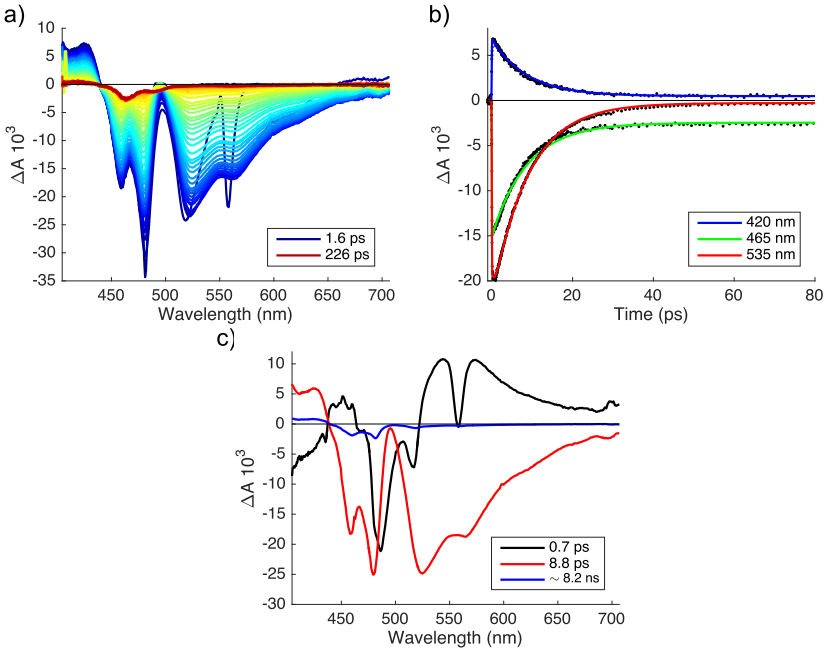

Figure 5.10: Vis-pump/vis-probe measurements for **1** in hexane: a) selected transient spectra; b) selected time-traces (black markers) and respective fits (color lines) produced by compartmental global analysis; c) decay-associated difference spectra (with time constants).

model LE$\xrightarrow{k^*}$LE$\xrightarrow{k_\gamma}$GS (Scheme 5.2). For this reason, the rate constants associated with vibrational relaxation and excited-state decay should be very close to $k^* = 1/\tau_1 = 1.511 \pm 0.008$ ps^{-1} and $k_\gamma = 1/\tau_2 = 0.1134 \pm 0.0001$ ps^{-1} that we obtain from global analysis.

Toluene. Three distinct regions can be observed in transient absorption measurements of **1** in toluene: ESA (415-450 nm), ground-state bleach (450-505 nm) and stimulated emission (510-680 nm). Selected transient spectra are shown in Fig. 5.11 a). Ground state bleach and stimulated emission signals are red-shifted relative to **1** in hexane, because toluene is more polar. The kinetics in toluene, as shown in Fig. 5.11 b), are much slower than in hexane. We attribute this to the increase in polarity that hinders excited-state deactivation through γ twist (Scheme 5.1 and Scheme 5.2).[2]

From global analysis of the whole transient data matrix we obtain two time constants of $\tau_1 = 2.7$ ps and $\tau_2 = 135.5$ ps. The DADS are shown in Fig. 5.11 c). The short component is associated with positive amplitude that is more pronounced at higher energies in the SE region, and its time constant shows a remarkable agreement with the solvent reorientation time reported for toluene.[24] The longer time constant is in good agreement with fluorescence decay data.[2] Transient spectroscopy in toluene shows excellent agreement with our previous work (Chapter

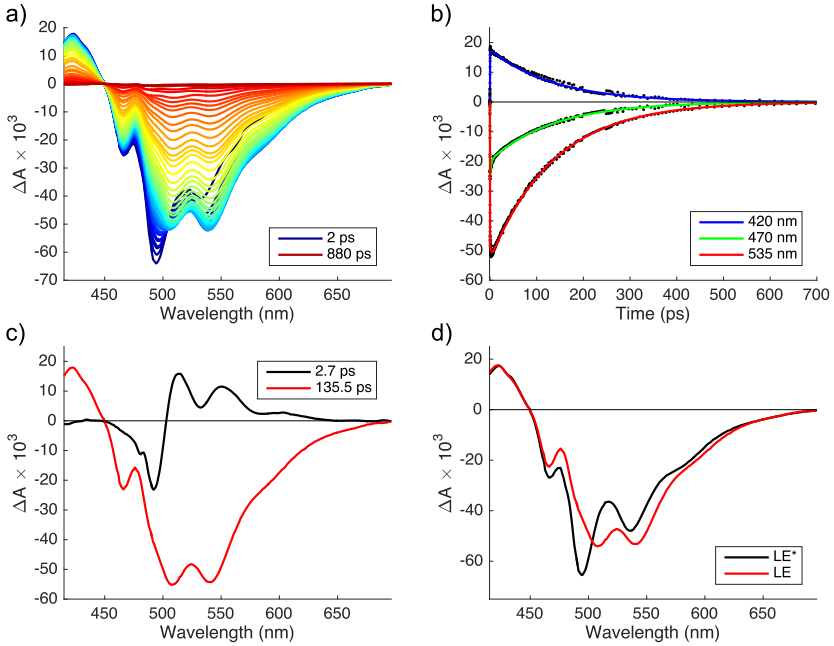

Figure 5.11: Vis-pump/vis-probe probe measurements for **1** in toluene: a) selected transient spectra; b) selected time-traces (black markers) and respective fits (color lines) produced by compartmental global analysis; c) decay-associated difference spectra (with time constants); d) species-associated difference spectra.

4),[2] where we attribute the shorter time constant to ultrafast solvation/vibrational cooling and the longer one to the decay of the LE state through conical intersection with the ground-state potential energy surface.

In order to model our data and obtain spectra associated with individual species, we assume the sequential model kinetics as illustrated in Scheme 5.2:

$$S_{1,\mathrm{LE}^*} \xrightarrow{k^*} S_{1,\mathrm{LE}} \xrightarrow{k_\gamma} S_0 \tag{5.7}$$

According to Eq. 5.7, photon absorption causes **1** to reach an electronically and vibrationally excited hot LE* state which rapidly relaxes to the planar LE state via vibrational cooling and solvation. Following relaxation, the molecule performs torsional motion involving the dicyanomethylene bond (γ in Scheme 5.1) and decays to the ground state. Global fit with the assumed sequential model produced time constants of $k^* = 0.3677 \pm (9 \times 10^{-4})$ ps^{-1} and $k_\gamma = 7.381 \times 10^{-3} \pm (3 \times 10^{-6})$ ps^{-1}. The reconstructed species-associated difference spectra are shown in Fig. 5.11 d).

Ethyl acetate. Excited-state dynamics of **1** in EtOAc is rather complex. EtOAc is just polar enough to enable TICT formation ($d_c(\epsilon) = 0.48$) and hinder excited-state deactivation through γ-twist (as we have inferred in ref. 2, and experimentally confirmed in this chapter), but it is not sufficiently polar to prevent

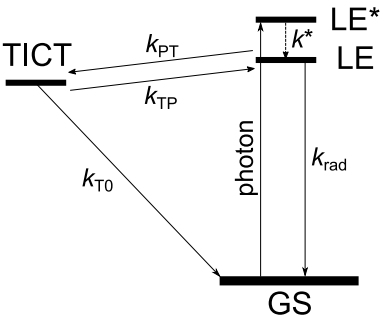

Scheme 5.3: Proposed model for excited-state deactivation of **1** through intermediate TICT-state formation in medium polar ($k_{TP} > 0$) and polar ($k_{TP} = 0$) solvents.

the back-conversion from the TICT state to the fluorescent LE state. Consequently, a considerable fraction of the total excited-state population occupies the non-fluorescent TICT state. The existence of a dark state is indicated in transient spectra measured at different delay times following the pump pulse (Fig. 5.12 a)). A time-trace measured at 480 nm (Fig. 5.12 b)) shows a pronounced rise component that correlates with decay of the signal measured at 535 nm (attributed to stimulated emission), and indicates formation of a dark intermediate that we associate with the β-twisted TICT geometry.[2] Global analysis of the transient data matrix produces time constants of $\tau_1 = 1.5$ ps, $\tau_2 = 30.3$ ps and $\tau_3 = 205.8$ ps. These values are in excellent agreement with the values that we obtain from fluorescence decay measurements at room temperature described in Chapter 4.[2] The reconstructed DADS is shown in Fig. 5.12. The shortest component shows a large amplitude in the SE region, which indicates ultra-fast solvation and/or vibrational relaxation. The second component (τ_2) shows a large negative amplitude in the SE region, and a large positive amplitude associated with this component in ground-state bleach region (Fig. 5.12). DADS associated with the longest time constant (τ_3) shows intense amplitude in GSB, and less intense amplitude in SE region.

Global analysis is, however, not able to provide an adequate interpretation in terms of the species that are involved in the relevant processes. For this reason, we model our transient data matrix by assuming that initial photoexcitation populates the hot LE* state which undergoes vibrational and solvent relaxation (k^*) to produce the fluorescent LE state. The LE state transforms into the dark TICT state (k_{PT}), through which ground-state repopulation takes place (k_{T0}). As the TICT state energetically lies very close to the LE state, the reverse reaction (k_{TP}) can take place and leads to delayed fluorescence that is observed in SE and fluorescence decay measurements. These processes are schematically shown in Scheme 5.3. In order to obtain species-associated difference spectra we fixed the values of respective rate constants (except k^*, which was optimized) to values previously obtained from fluorescence decay measurements (see Table 4.2) at room temperature:

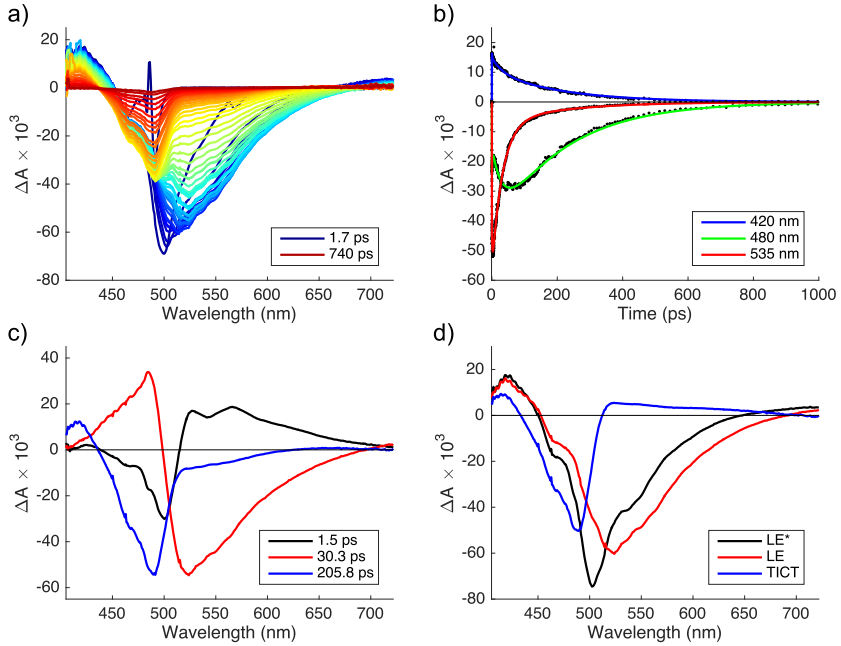

Figure 5.12: Vis-pump/vis-probe probe measurements for **1** in EtOAc: a) selected transient spectra; b) selected time-traces (black markers) and respective fits (color lines) produced by compartmental global analysis; c) decay-associated difference spectra (with time constants); d) species-associated difference spectra.

$k^* = 0.691 \pm (2 \times 10^{-3})$ ps^{-1} (optimized parameter), $k_{\mathrm{PT}} = 2.53 \times 10^{-2}$ ps^{-1} (fixed parameter), $k_{\mathrm{TP}} = 4.78 \times 10^{-3}$ ps^{-1} (fixed parameter) and $k_{\mathrm{T0}} = 5.84 \times 10^{-3}$ ps^{-1} (fixed parameter). The resulting species-associated difference spectra are shown in Fig. 5.12 d) and selected time-traces with produced fits are shown in Fig. 5.12 b).

Acetonitrile. Excited-state dynamics of **1** is very fast, and formation of the dark state can be observed in both spectral and time-traces (see Fig. 5.13 a) and b)). Global analysis produces time-constants $\tau_1 = 0.5$ ps, $\tau_2 = 6.2$ ps and $\tau_3 = 10.4$ ps. These time constants are attributed to solvation/vibrational relaxation,[24] conversion of the planar LE state into the TICT state and decay of the TICT state, respectively. The reconstructed DADS (Fig. 5.13 c)) looks similar to the one obtained in EtOAc and indicates sequential dynamics of the TICT state formation (Scheme 5.3).

We model the transient data matrix by assuming sequential kinetics:

$$S_{1,\mathrm{LE}^*} \xrightarrow{k^*} S_{1,\mathrm{LE}} \xrightarrow{k_{\mathrm{PT}}} S_{1,\mathrm{TICT}} \xrightarrow{k_{\mathrm{T0}}} S_0 \tag{5.8}$$

which produces the rate constants of $k^* = 2.201 \pm (6 \times 10^{-3})\ ^{-1}$, $k_{\mathrm{PT}} = 0.1613 \pm (3 \times 10^{-4})\ ^{-1}$, $k_{\mathrm{T0}} = 0.09637 \pm (2 \times 10^{-4})$ ps^{-1}.

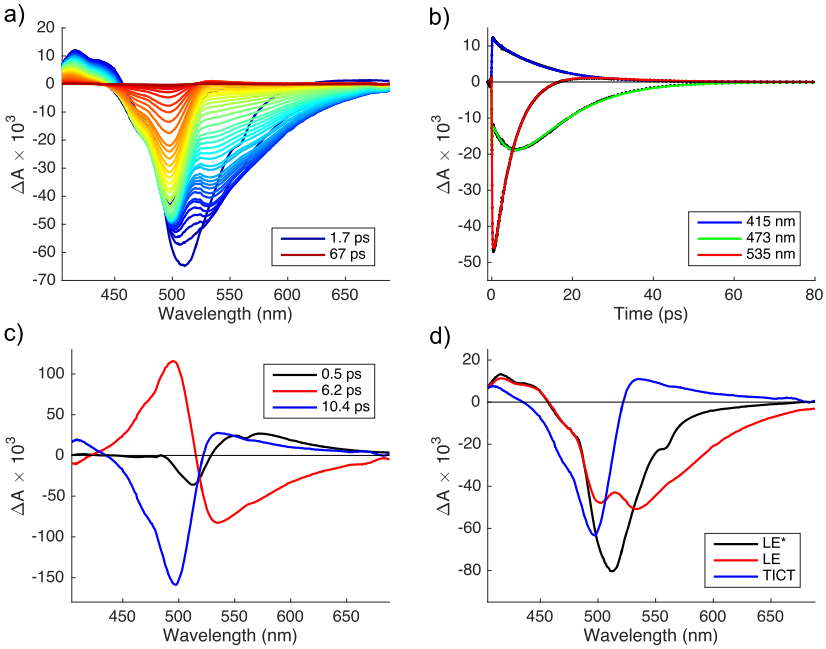

Figure 5.13: Vis-pump/vis-probe probe measurements for **1** in MeCN: a) selected transient spectra; b) selected time-traces (black markers) and respective fits (color lines) produced by compartmental global analysis; c) decay-associated difference spectra (with time constants); d) species-associated difference spectra.

Dimethylsulfoxide. Excited-state kinetics of **1** is DMSO is mechanistically identical to the one observed in MeCN, but slower. We attribute this slowdown to increased viscosity of DMSO ($\eta = 1.99$[9] mPa s) relative to MeCN ($\eta = 0.35$[9] mPa s), due to which we would expect the nonradiative rate of **1** in DMSO to be 3.7× slower relative to MeCN ($\sim$ 23 ps), according to the hydrodynamic theory. As for **1** in DMSO, formation of the dark TICT state is indicated by a pronounced delay between the ground-state bleach signal recovery and stimulated emission, as shown in Figs. 5.14 a) and b). Global analysis produces time-constants of $\tau_1 = 1.30$ ps, $\tau_2 = 12.05$ ps and $\tau_3 = 29.12$ ps, and these values are in excellent agreement with the time-constants obtained in our previous work described in Chapter 4.[2] The reconstructed DADS shown in Fig. 5.14 c) and its features are similar to other measurements where the TICT formation takes place (see above). We once again model the transient data matrix according to sequential model illustrated in Scheme 5.3 and Eq. 5.8 and obtain rate constants $k^* = 0.768 \pm 5 \times (10^{-3})$ ps^{-1}, $k_{\mathrm{PT}} = 3.434 \times 10^{-2} \pm (6 \times 10^{-5})$ ps^{-1} and $k_{\mathrm{T0}} = 8.30 \times 10^{-2} \pm (3 \times 10^{-4})$ ps^{-1}. The reconstructed species-associated difference spectra shown in Fig. 5.14 d), shows features that are similar to those obtained for **1** in MeCN.

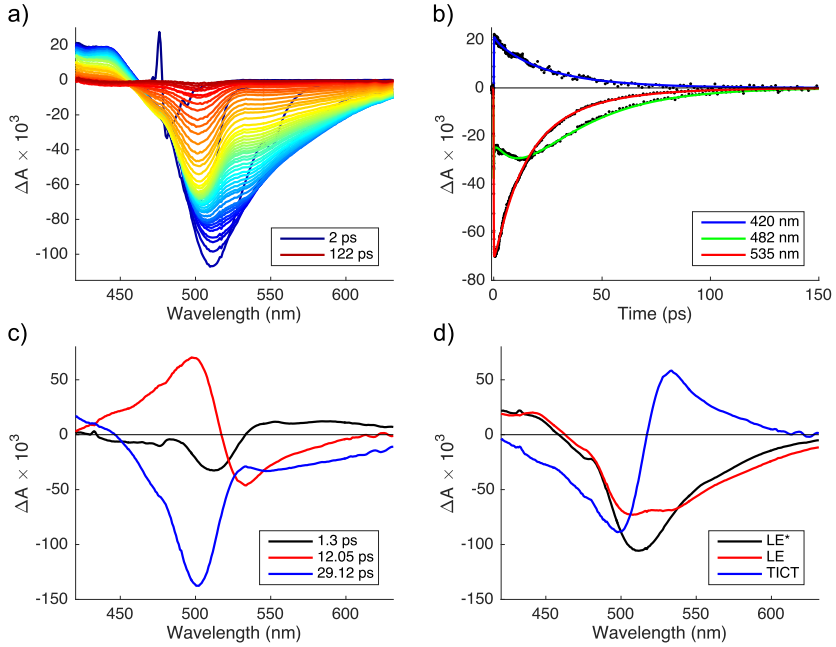

Figure 5.14: Vis-pump/vis-probe probe measurements for **1** in DMSO: a) selected transient spectra; b) selected time-traces (black markers) and respective fits (color lines) produced by compartmental global analysis; c) decay-associated difference spectra (with time constants); d) species-associated difference spectra.

5.3.5 Conclusion

Fast nonradiative decay through a twisting motion is the basis for application of molecular rotors such as **1** to viscosity sensing. Excited-state deactivation of **1** takes place through two different pathways with the opposite response to solvent polarity. Our results show that in a certain range of solvent polarities both twisting modes are relatively slow, and **1** is not as effective as a viscosity probe. We suspect that a similar situation may also apply to other viscosity probes such as 9-(2,2-dicyanovinyl)julolidine.

5.4 Appendix to Chapter 5

5.4.1 Dielectric properties of MTHF as a function of temperature

Refractive indices of MTHF at different temperatures have been calculated from experimentally determined densities reported in ref. 7 according to the Lorentz-

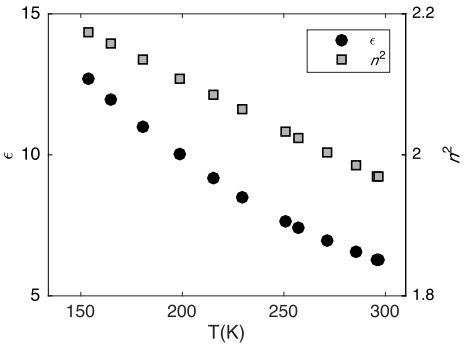

Figure 5.15: Relative permitivitty ϵ and refractive index n of MTHF as a function of temperature (from ref. 7).

Lorentz expression:[25]

$$\frac{n^2-1}{n^2+2}\frac{M}{\rho} = \frac{N_A\alpha}{3\epsilon_0}, \tag{5.9}$$

where n is the refractive index of the solvent, M the molecular weight, ρ the density, N_A Avogadro's number, ϵ_0 is the vacuum permittivity, and α is the molecular polarizability of MTHF. We obtain this number from literature value of the refractive index at 293 K ($n = 1.4059$). Such data has been interpolated/extrapolated according to the expression:

$$n(T) = A + BT, \tag{5.10}$$

where A and B represent constants obtained through linear fit of the experimental data, and T represents the temperature (in K). The values we obtain are $A = 1.552$ and $B = -5.01 \times 10^{-4}$.

Dielectric constants were obtained from the data reported in ref. 7 by fitting a second order polynomial:

$$\epsilon(T) = A + BT + CT^2, \tag{5.11}$$

where A, B and C are constants. We obtain the following values for these parameters: $A = 26.77$, $B = -0.1157$ and $C = 1.57 \times 10^{-4}$.

Functions that account for a full dielectric response of the solvent $d_c(\epsilon)$ and electronic polarization $d_c(n^2)$ (see Chapter 2.1.5 for details) have been calculated from refractive indices n and relative permitivitties ϵ obtained as described above.[5,6] Values for solute cavity radius and solute polarizability we use here are identical to the ones reported in Chapter 4.3.1.[2] The values of relative permittivities ϵ and refractive indices n are shown in Fig. 5.15 for the examined temperature range. The solvent orientational polarization was obtained by subtracting the effect of electronic polarization from a full dielectric response of the solvent, and these values are shown in Fig 5.16. In Figs. 5.15 and 5.16 gray squares represent the region where interpolation of the experimental data is not valid, because the solvent freezes ($d_c(\epsilon) = d_c(n^2)$).

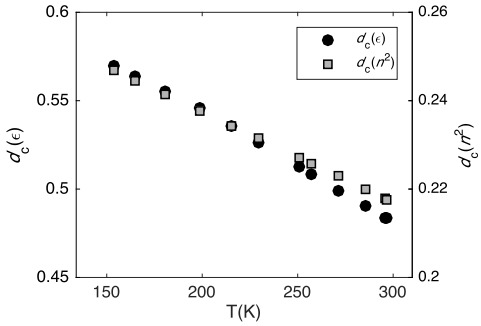

Figure 5.16: Dielectric properties of MTHF as a function of temperature (from ref. 7).

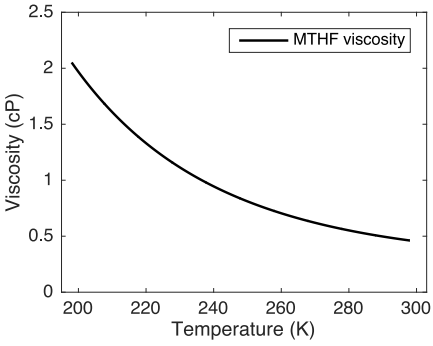

Figure 5.17: Viscosity of MTHF as a function of temperature (from ref. 7).

5.4.2 Viscosity of MTHF as a function of temperature

Viscosities of MTHF as a function of temperature between 198 K and 298 K have been reported in ref. 7. Interpolated values of viscosity (second order polynomial) as a function of temperature between 198 K and 298 K are shown in Fig 5.17.

5.4.3 Fluorescence decays of **1** in toluene/MeCN mixtures

Fluorescence decays of **1** in pure toluene and MeCN are monoexponential. In the examined toluene/MeCN, fluorescence decays show biexponential behavior. Amplitudes and fluorescence decay rates obtained by biexponential fit of the fluorescence decay curves are shown in Fig. 5.19 a) and b), respectively. Fluorescence decays measured for solutions in which the solvent polarity comes close to the polarity of MeCN were not taken into consideration in our analysis (see Section 5.3.3), because fluorescence lifetimes of such samples are too short to be measured with our TCSPC setup.

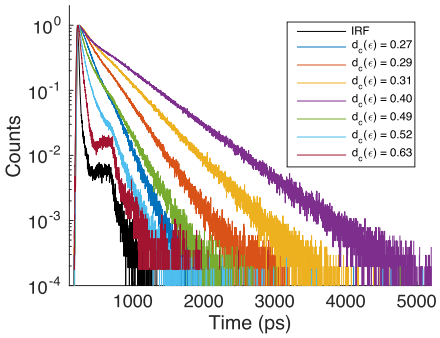

Figure 5.18: Representative TCSPC curves of **1** in pure toluene ($d_c(\epsilon) = 0.27$), toluene/MeCN mixtures, and pure MeCN ($d_c(\epsilon) = 0.63$).

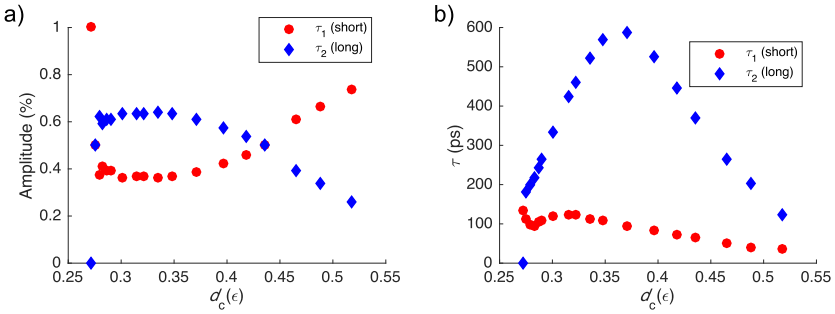

Figure 5.19: a) Fluorescence lifetimes and b) amplitudes of **1** obtained by fitting TCSPC data in toluene/MeCN mixtures.

5.4.4 DCVJ polarity response

Maroncelli's group found strong indications that the nonradiative decay of 9-(2,2-dicyanovinyl)julolidine (DCVJ) depends, in addition to solvent viscosity, on solvent polarity in the low-viscosity regime.[6] In 2014 Gaffney's group showed that excited-state decay in polar DMSO occurs via branching,[26] in which both rotation around a formally single and double bonds play an important role (Fig. 5.20 a)). Because of a large degree of functional similarity between DCVJ and DCDHF molecular rotors, these results motivated us to conduct a preliminary experiment where we titrate the toluene solution of DCVJ with DMSO. Our current data show that fluorescence quantum yields of DCVJ increase upon addition of small volumes of DMSO, and then continue to slowly decrease (Fig. 5.20 b)) as more DMSO is added. Such trend indicates that DCVJ shows solvent polarity-dependent behavior similar to that of **1**.

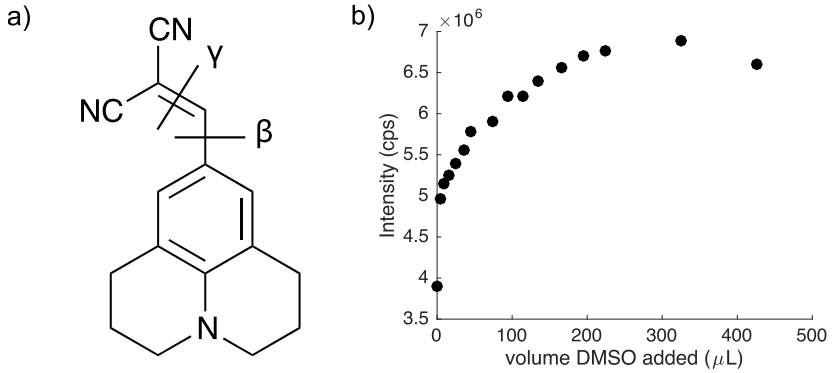

Figure 5.20: a) Molecular structure of DCVJ and relevant twists; b) Fluorescence intensity of DCVJ in toluene (3 mL) as a function of added DMSO.

References

1. Suhina, T.; Weber, B.; Carpentier, C. E.; Lorincz, K.; Schall, P.; Bonn, D.; Brouwer, A. M. *Angew. Chem. Int. Ed.* **2015**, *54*, 3688–3691.
2. Suhina, T.; Amirjalayer, S.; Mennucci, B.; Woutersen, S.; Hilbers, M.; Bonn, D.; Brouwer, A. M. *J. Phys. Chem. Lett.* **2016**, *7*, 4285–4290.
3. Gubler, U.; He, M.; Wright, D.; Roh, Y.; Twieg, R.; Moerner, W. *Adv. Mater.* **2002**, *14*, 313–317.
4. Lakowicz, J. R. *Principles of Fluorescence Spectroscopy*; Springer Science & Business Media, 2006.
5. Dahl, K.; Biswas, R.; Ito, N.; Maroncelli, M. *J. Phys. Chem. B* **2005**, *109*, 1563–1585.
6. Jin, H.; Liang, M.; Arzhantsev, S.; Li, X.; Maroncelli, M. *J. Phys. Chem. B* **2010**, *114*, 7565–7578.
7. Nicholls, D.; Sutphen, C.; Szwarc, M. *J. Phys. Chem.* **1968**, *72*, 1021–1027.
8. Zoon, P. D.; Brouwer, A. M. *Photochem. Photobiol. Sci.* **2009**, *8*, 345–353.
9. Haynes, W. M. *CRC handbook of chemistry and physics*; CRC press, 2014.
10. Reichardt, C.; Welton, T. *Solvents and solvent effects in organic chemistry*; John Wiley & Sons, 2011.
11. Valeur, B.; Berberan-Santos, M. N. *Molecular fluorescence: principles and applications*; John Wiley & Sons, 2012.
12. Zoon, P. D.; Brouwer, A. M. *ChemPhysChem* **2005**, *6*, 1574–1580.
13. Dreger, Z.; Lang, J.; Drickamer, H. *Chem. Phys.* **1992**, *166*, 193–206.
14. Ritzoulis, G.; Papadopoulos, N.; Jannakoudakis, D. *J. Chem. Eng. Data* **1986**, *31*, 146–148.
15. Shams, A. K. *J. Al-Nahrain Univ.* **2011**, *14*, 75–85.
16. Rettig, W. *J. Phys. Chem.* **1982**, *86*, 1970–1976.

17. Mullen, K. M.; Van Stokkum, I. H. *J. Stat. Softw.* **2007**, *18*, 1–46.
18. Snellenburg, J.; Laptenok, S.; Seger, R.; Mullen, K.; Van Stokkum, I. *J. Stat. Softw.* **2012**, *49*.
19. Willets, K. A.; Ostroverkhova, O.; He, M.; Twieg, R. J.; Moerner, W. *J. Am. Chem. Soc.* **2003**, *125*, 1174–1175.
20. Willets, K. A.; Callis, P. R.; Moerner, W. *J. Phys. Chem. B* **2004**, *108*, 10465–10473.
21. Lord, S. J.; Lu, Z.; Wang, H.; Willets, K. A.; Schuck, P. J.; Lee, H.-l. D.; Nishimura, S. Y.; Twieg, R. J.; Moerner, W. *J. Phys. Chem. A* **2007**, *111*, 8934–8941.
22. Lord, S. J.; Conley, N. R.; Lee, H.-l. D.; Samuel, R.; Liu, N.; Twieg, R. J.; Moerner, W. *J. Am. Chem. Soc.* **2008**, *130*, 9204–9205.
23. Lord, S. J.; Conley, N. R.; Lee, H.-l. D.; Nishimura, S. Y.; Pomerantz, A. K.; Willets, K. A.; Lu, Z.; Wang, H.; Liu, N.; Samuel, R.; Weber, R.; Semyonov, A.; He, M.; Twieg, R. J.; Moerner, W. E. *ChemPhysChem* **2009**, *10*, 55–65.
24. Horng, M.-L.; Gardecki, J.; Maroncelli, M. *J. Phys. Chem. A* **1997**, *101*, 1030–1047.
25. Lorenz, L. *Ann. Phys.* **1880**, *247*, 70–103.
26. Zhang, W.; Lan, Z.; Sun, Z.; Gaffney, K. J. *J. Phys. Chem. B* **2012**, *116*, 11527–11536.